



MIT Open Access Articles

Quantum enhanced LIDAR resolution with multi-spatial-mode phase sensitive amplification

The MIT Faculty has made this article openly available. **Please share** how this access benefits you. Your story matters.

Citation	Cesar A. Santivanez ; Saikat Guha ; Zachary Dutton ; Muthiah Annamalai ; Michael Vasilyev ; Brent J. Yen ; Ranjith Nair ; Jeffrey H. Shapiro; Quantum enhanced lidar resolution with multi-spatial-mode phase sensitive amplification. Proc. SPIE 8163, Quantum Communications and Quantum Imaging IX, 81630Z (September 06, 2011). SPIE © 2011
As Published	http://dx.doi.org/10.1117/12.903351
Publisher	SPIE
Version	Final published version
Citable link	http://hdl.handle.net/1721.1/73931
Terms of Use	Article is made available in accordance with the publisher's policy and may be subject to US copyright law. Please refer to the publisher's site for terms of use.

Quantum enhanced LIDAR resolution with multi-spatial-mode phase sensitive amplification

Cesar A. Santivanez^a, Saikat Guha^a, Zachary Dutton^a, Muthiah Annamalai^b, Michael Vasilyev^b, Brent J. Yen^c, Ranjith Nair^c, and Jeffrey H. Shapiro^c

^aRaytheon BBN Technologies
10 Moulton St., Cambridge, MA 02138, USA;

^bDept. of Electrical Engineering, Univ. of Texas-Arlington
416 Yates St., Arlington, TX 76019, USA;

^cResearch Laboratory of Electronics, Massachusetts Institute of Technology
77 Massachusetts Ave, Cambridge, MA 02139, USA

ABSTRACT

Phase-sensitive amplification (PSA) can enhance the signal-to-noise ratio (SNR) of an optical measurement suffering from detection inefficiency. Previously, we showed that this increased SNR improves LADAR-imaging spatial resolution when infinite spatial-bandwidth PSA is employed. Here, we evaluate the resolution enhancement for realistic, finite spatial-bandwidth amplification. PSA spatial bandwidth is characterized by numerically calculating the input and output spatial modes and their associated phase-sensitive gains under focused-beam pumping. We then compare the spatial resolution of a baseline homodyne-detection LADAR system with homodyne LADAR systems that have been augmented by pre-detection PSA with infinite or finite spatial bandwidth. The spatial resolution of each system is quantified by its ability to distinguish between the presence of 1 point target versus 2 closely-spaced point targets when minimum error-probability decisions are made from quantum limited measurements. At low (5-10 dB) SNR, we find that a PSA system with a 2.5kWatts pump focused to $25\mu\text{m} \times 400\mu\text{m}$ achieves the same spatial resolution as a baseline system having 5.5 dB higher SNR. This SNR gain is very close to the 6 dB SNR improvement possible with ideal (infinite bandwidth, infinite gain) PSA at our simulated system detection efficiency (0.25). At higher SNRs, we have identified a novel regime in which finite spatial-bandwidth PSA outperforms its infinite spatial-bandwidth counterpart. We show that this performance crossover is due to the focused pump system's input-to-output spatial-mode transformation converting the LADAR measurement statistics from homodyne to heterodyne performance.

Keywords: Phase-Sensitive Amplification (PSA), multi-mode PSA, LIDAR, homodyne detection

1. INTRODUCTION

For modest-range (1–100 km) terrestrial applications under clear-weather conditions, LADAR (LAsER Detection And Ranging) systems^{1,2} offer superior spatial resolution, when compared to microwave radars, owing to their use of much shorter wavelengths. When atmospheric turbulence can be neglected, the spatial resolution of such a system is generally limited by the Rayleigh resolution of its receiving optics ($1.22\lambda/D$, where λ is the LADAR wavelength and D is the aperture diameter for an unobscured circular entrance pupil) and the signal-to-noise ratio (SNR).

In our previous work³ we showed that Phase-Sensitive Amplification (PSA) can enhance the signal-to-noise ratio (SNR) of an optical measurement suffering from detection inefficiency, when infinite spatial-bandwidth PSA is employed. For sufficiently high PSA gain (G_{eff}), a PSA-enhanced detector can recover the losses due to a detector efficiency $\eta < 1$. In this paper, we evaluate the resolution enhancement for realistic, finite spatial-bandwidth amplification. To this end, we characterize the PSA crystal by numerically calculating the most significant input and output spatial modes and their associated phase-sensitive gains under focused-beam

Corresponding author: Dr. Cesar. A. Santivanez, e-mail: csantiva@bbn.com

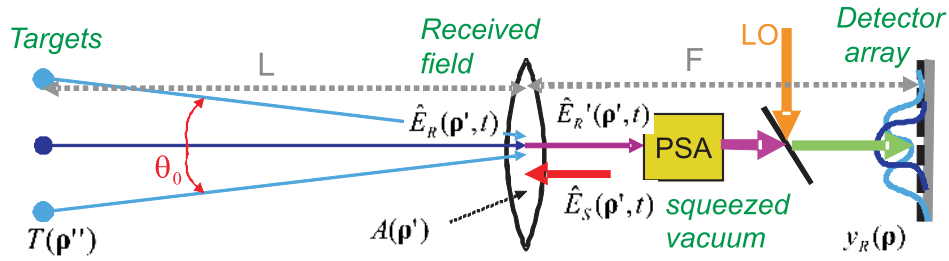


Figure 1: (Color online) Diagram of our quantum enhanced LADAR receiver. At the far left we show the targets (at range L from the receiver) considered in the resolution analysis—one point target on axis and two point targets symmetrically disposed at $\pm\theta_0$ in angle about the optical axis. The baseband photon-units field operator \hat{E}_R of the target return is transmitted through a spatially-dependent (soft) aperture $A(\boldsymbol{\rho}')$, and a squeezed-vacuum field operator \hat{E}_S is injected. The resulting field operator \hat{E}'_R then undergoes phase-sensitive amplification before being mixed with a local oscillator and homodyne detected. Note that for clarity sake, in this paper we are **not** considering the SVI input. We consider a one-dimension homodyne-detection array. This quantum-enhanced receiver will be compared with a classical baseline LADAR system in which \hat{E}_S is in its vacuum state and no PSA is employed.

pumping. We then compare the spatial resolution of a baseline homodyne-detection LADAR system against homodyne LADAR systems that have been augmented by pre-detection PSA with infinite or finite spatial bandwidth. The spatial resolution of each system is quantified by its ability to distinguish between the presence of 1 point target versus 2 closely-spaced point targets when minimum error-probability decisions are made from quantum limited measurements. Interestingly we find the performance of our finite spatial bandwidth device can actually surpass the performance of a flat-phase infinite bandwidth device. While one may have expected an infinite bandwidth device to be superior, a device that amplifies all spatial modes in the same quadrature is not optimal. Our detailed modeling reveals that the modal phase conjugation which occurs in a PSA device has an important and in many cases positive effect on the performance. When we refer to the “infinite bandwidth” approximation in this paper, we specifically refer to a device in which all modes are amplified equally and with uniform phase matched to homodyne measurement quadrature. Our results show the existence of 3 regimes:

- At low SNR, a finite-spatial bandwidth PSA is able to recover the losses due to detection inefficiency. Moreover, under realistic pixel sizes, the performance obtained by using a finite-spatial-bandwidth PSA is slightly better than the performance predicted by employing the “infinite-bandwidth” approximation.
- At medium SNR, the spatial-bandwidth PSA performance is worse than the performance predicted using the “infinite-bandwidth” approximation.
- At high SNR, the realistic, finite-bandwidth PSA significantly outperforms the expectation due to the “infinite-bandwidth” model. The PSA-enhanced homodyne detector performance asymptotically tracks that of a heterodyne detector.

The remainder of this paper is organized as follows. In Section 2 we describe our LADAR receiver configuration. In Section 3 we describe the modal decomposition for the finite-bandwidth PSA. In Section 4 we derive the expressions for the statistics of the homodyne measurements and the optimal decision theory. In Section 5 we show numerical results obtained through Monte Carlo simulations. In Section 6 we conclude the paper with some discussion about future work.

2. LADAR RECEIVER CONFIGURATION

A simple schematic of our quantum-enhanced LADAR receiver concept is shown in Figure 1. Not shown is the LADAR transmitter that floodlights the target region with a pulse of laser light. This is the same setup as the one utilized in.³ For clarity of the discussion, in this paper we remove the SVI input, and for maximum realism

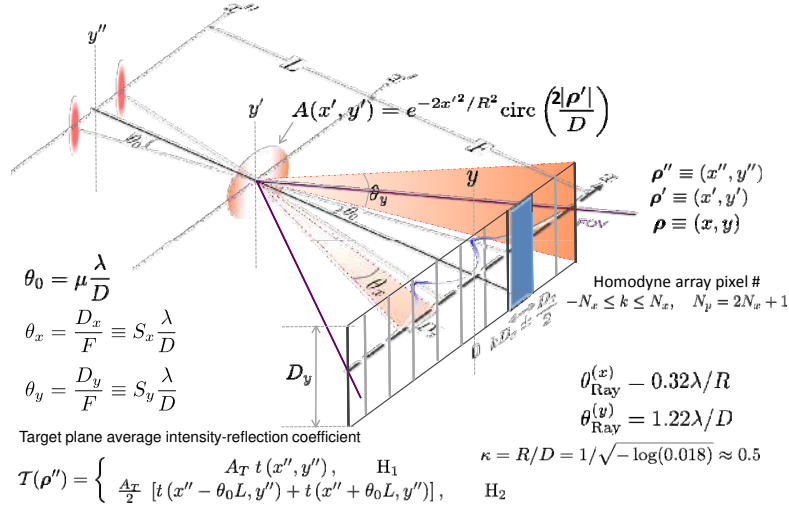


Figure 2: Homodyne detector-array geometry.

we consider discrete-size pixels and a precise modeling of the PSA operation. Furthermore, to better match the one-dimension detector array, we utilize a one-dimension soft-aperture embedded in a hard aperture, which results in a aperture transmission mask with field transmittance $A(x', y') = e^{-\frac{2x'^2}{R^2}} \text{circ}\left(\frac{2|\rho'|}{D}\right)$, where R is the soft-aperture beam width, and D is the hard-aperture diameter.

The PSA crystal has non-negligible length, which introduces diffraction effects. To compensate this, lenses (not shown) are used so that the desired signal is focused at the center of the PSA crystal. Similarly, lenses at the PSA output reverse the crystal diffraction, such that the image focused on the detector array is the same as the signal at the center of the PSA. The combined effect is that the PSA can be modeled as zero-length (i.e. a vertical plane), with the measurements taken at the right side (exit) of that plane.

With the above caveats, the system in Figure 1 can be modeled as shown in Figure 2. The PSA is modeled as a zero-length plane just before the detector array of N_p pixels (labeled $-N_x, \dots, 0, \dots, N_x$ with $N_p = 2N_x + 1$). Table 1 lists the quantities used in this paper along with their notation. Note the introduction of “dimensionless” units μ , S_x , and S_y .

3. PSA MODAL DECOMPOSITION

The PSA spatial-temporal modes are characterized by three complete orthonormal (CON) mode sets:

- Input spatial CON mode set: $\{\Phi_n(\boldsymbol{\rho})\}$, $\boldsymbol{\rho} \in \text{PSA input facet}$.
- Output spatial CON mode set: $\{\phi_n(\boldsymbol{\rho})\}$, $\boldsymbol{\rho} \in \text{PSA output facet}$.
- Temporal CON mode set: $\{\xi_m(t)\}$, $t \in [2L/c, 2L/c + \tau_p]$.

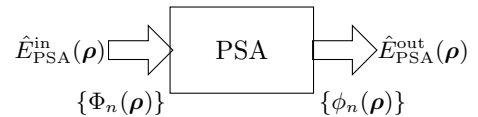


Figure 3: PSA modal decomposition.

It turns out that when the PSA is focused at the center plane of the crystal, the output modes are simply related to the input modes by a complex conjugation operation, i.e. :

$$\phi_n(\boldsymbol{\rho}) = \Phi_n(\boldsymbol{\rho})^*$$

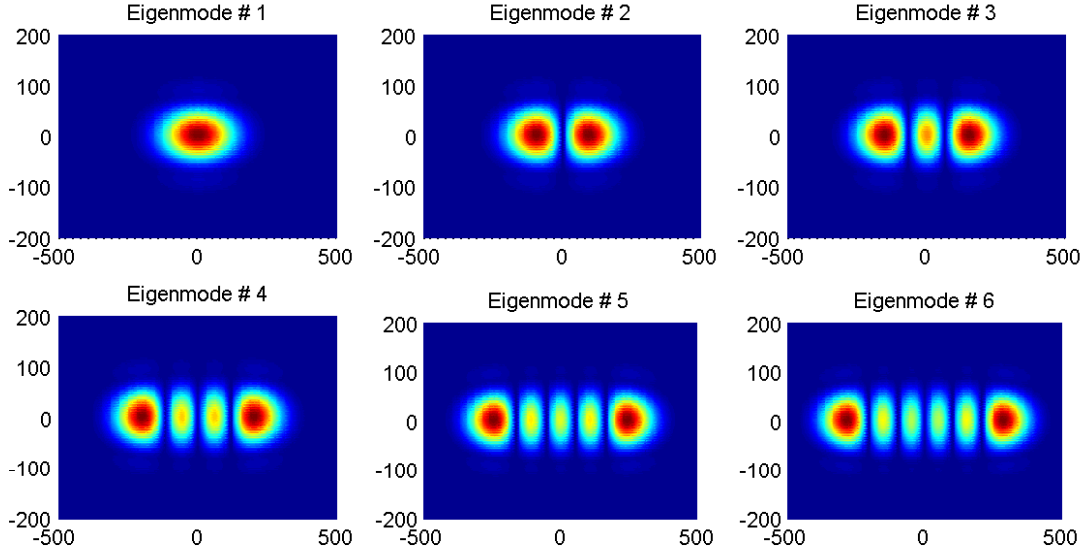


Figure 4: (Color Online) The 6 most amplified eigenmodes (absolute value). The coordinates unit is μm

Then the PSA model decomposition is:

$$\hat{E}_{\text{PSA}}^{\text{in}}(\boldsymbol{\rho}, t) = \sum_{n,m} \hat{a}_{nm}^{\text{in}} \Phi_n(\boldsymbol{\rho}) \xi_m(t) \quad (1)$$

$$\hat{E}_{\text{PSA}}^{\text{out}}(\boldsymbol{\rho}, t) = \sum_{n,m} \hat{a}_{nm}^{\text{out}} \phi_n(\boldsymbol{\rho}) \xi_m(t) \quad (2)$$

$$\hat{a}_{nm}^{\text{out}} = \sqrt{g_n} \hat{a}_{nm}^{\text{in}} + \sqrt{g_n - 1} (\hat{a}_{nm}^{\text{in}})^\dagger, \quad (3)$$

where the input $\hat{E}_{\text{PSA}}^{\text{in}}(\boldsymbol{\rho}, t)$ is a vacuum-state field, $g_n \geq 1$ is the gain parameter for the n -th spatial mode (i.e., $G_{\text{eff},n}$, the PSA quadrature gain associated with the n -th most amplified mode, is equal to $G_{\text{eff},n} = (\sqrt{g_n} + \sqrt{g_n - 1})^2$). Note that we have suppressed propagation delays within the receiver, and we have assumed that the PSA has a temporal bandwidth that greatly exceeds $1/\tau_p$. We can choose any temporal CON set, so use $\xi_1(t) = s(t - 2L/c - F/c)$, which allows us, because we will ultimately be matched filtering for $\xi_1(t)$, to deal solely with the pure spatially-dependent field operators.

The shape of the (most amplified) eigenmodes is dependent on the pump size and power. These eigenmodes were computed numerically using the methodology described in.⁴⁻⁷ Figure 4 shows the first six eigenmodes (amplitude) for a $400\mu m \times 25\mu m$ elliptical pump with a power of 2.5KWatts. Figure 5 show the different gains $G_{\text{eff},n}$ for the first 50 eigenmodes. It can be seen that the gains quickly converge to 1. Thus, there is little value in considering eigenmodes with indices above 50. Furthermore, we also noticed that for our soft-aperture and focusing most of the target signal is covered by the first 50 eigenmodes. Then, for $n = 51, 52, \dots$ we can safely assume that $g_n = 1$, and $\phi_n(\boldsymbol{\rho}) = \Phi_n(\boldsymbol{\rho})$ (i.e. eigenmodes are real).

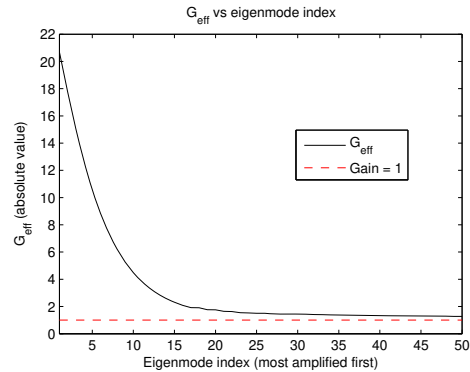


Figure 5: PSA quadrature gain ($G_{\text{eff},n}$) for the 50 most amplified eigenmodes. The gains quickly approach 1.

Var.	Description	Var.	Description
$\boldsymbol{\rho}''$	A point in the target plane	$\boldsymbol{\rho}'$	A point in the pupil plane (where the aperture is)
$\boldsymbol{\rho}$	A point in the image plane (where the detector array is)	L	Target range (i.e., distance from target plane to the pupil plane)
F	Distance from the pupil plane to the image plane	θ_0	Angular separation under the two-target hypothesis
λ	LADAR wavelength	c	Speed of light
R	Beam width of the soft-aperture	D	Diameter of the hard aperture
N_p	Number of pixels ($N_p = 2N_x + 1$)	N_x	Highest pixel index
D_x	Pixel width	D_y	Pixel height
$\theta_{Ray}^{(x)}$	Aperture's Rayleigh resolution in the X-dimension, equal to $0.32\lambda/R$	$\theta_{Ray}^{(y)}$	Aperture's Rayleigh resolution in the Y-dimension, equal to $1.22\lambda/D$
κ	Ratio $\frac{R}{D}$	μ	Angular separation in dimensionless units
S_x	Pixel width in dimensionless units	S_y	Pixel height in dimensionless units
A_T	LADAR cross-section of the single point target	I_T	Target plane intensity (in W/m^2) produced by the transmitter pulse
τ_p	pulse duration	$\hbar\omega_\lambda$	Photon energy at the LADAR wavelength
$s(t)$	Normalized baseband shape of the transmitter pulse	$T(\boldsymbol{\rho}'')$	Target's field-reflection coefficient
$\mathcal{T}(\boldsymbol{\rho}'')$	Target average intensity-reflection coefficient	$A(\boldsymbol{\rho}')$	Soft-aperture transmission mask field transmittance
$m(\boldsymbol{\rho})$	Soft-aperture point-spread function (PSF): $m(\boldsymbol{\rho}) = \int A(\lambda F \mathbf{f}) e^{i2\pi \mathbf{f} \cdot \boldsymbol{\rho}} d\mathbf{f}$	η	Homodyne detector quantum efficiency
$\hat{E}_{PSA}^{\text{in}}(\boldsymbol{\rho}, t)$	PSA-input field operator	$\hat{E}_{PSA}^{\text{out}}(\boldsymbol{\rho}, t)$	PSA-output field operator

Table 1: Notation for the quantities used in this paper.

4. HOMODYNE DETECTOR MEASUREMENT STATISTICS

We assume two equally-likely hypotheses: one on-axis speckle point target (H_1) or two off-axis speckle point targets (H_2). Under H_2 , the point targets are symmetrically placed at angles $\pm\theta_0$ about the optical axis and have statistically independent speckle behavior. We assume that the targets return the same average power to the LADAR receiver under each hypothesis. The average intensity-reflection coefficient is:

$$\mathcal{T}(\boldsymbol{\rho}'') = \begin{cases} A_T \delta(\boldsymbol{\rho}''), & \text{under } H_1 \\ (A_T/2)[\delta(\boldsymbol{\rho}'' - \theta_0 L \mathbf{i}_{x''}) + \delta(\boldsymbol{\rho}'' + \theta_0 L \mathbf{i}_{x''})], & \text{under } H_2, \end{cases} \quad (4)$$

where A_T and L are defined in Table 1 and $\mathbf{i}_{x''}$ is the x'' -axis unit vector. A 1-D detector array stretched along the x -axis generates the following homodyne detection statistic $\mathbf{y} = [y_{-N_x} \cdots y_{N_x}]^T$, where y_n is the matched-filter output for the n -th detector. The binary hypothesis test is

$$\begin{aligned} H_1 : \quad \mathbf{y} &= \mathbf{s}^{(1)} + \mathbf{w} \sim N(\mathbf{0}, \boldsymbol{\Lambda}_1) \\ H_2 : \quad \mathbf{y} &= \mathbf{s}^{(2)} + \mathbf{w} \sim N(\mathbf{0}, \boldsymbol{\Lambda}_2), \end{aligned}$$

where $\mathbf{s}^{(k)} = [s_{-N_x}, \dots, s_{N_x}]^T$ is the target-return component, $\mathbf{w} = [w_{-N_x}, \dots, w_{N_x}]^T$ is the noise component, and the covariance matrix under H_k is $\boldsymbol{\Lambda}_k = E[\mathbf{y}\mathbf{y}^T | H_k]$, $k = 1, 2$. Under each hypothesis, $\mathbf{s}^{(k)}$ and \mathbf{w} are

independent, zero-mean, Gaussian random vectors. The optimal ML decision rule is

$$\mathbf{y}^T \left[\mathbf{\Lambda}_1^{-1} - \mathbf{\Lambda}_2^{-1} \right] \mathbf{y} \begin{array}{l} \text{decide } H_2 \\ \geq \\ < \\ \text{decide } H_1 \end{array} \ln \left(\frac{|\mathbf{\Lambda}_2|}{|\mathbf{\Lambda}_1|} \right), \quad (5)$$

where $|\mathbf{\Lambda}_k|$ denotes the determinant of $\mathbf{\Lambda}_k$. In this section we derive expressions for $\mathbf{\Lambda}_1$ and $\mathbf{\Lambda}_2$.

4.1 PSA input

The LADAR transmitter emits coherent-state light, so we take the target return to be a classical field

$$E_R(\boldsymbol{\rho}', t) = \int \sqrt{\frac{I_T \tau_p}{\hbar \omega}} s(t - 2L/c) T(\boldsymbol{\rho}'') \frac{e^{-ik\boldsymbol{\rho}' \cdot \boldsymbol{\rho}''/L + ik|\boldsymbol{\rho}'|^2/2L}}{i\lambda L} d\boldsymbol{\rho}'', \quad (6)$$

where the exponential represents Fraunhofer diffraction from position $\boldsymbol{\rho}''$ in the target plane to position $\boldsymbol{\rho}'$ in the pupil plane, and

$$s(t) = \begin{cases} 1/\sqrt{\tau_p}, & \text{for } 0 \leq t \leq \tau_p \\ 0, & \text{otherwise} \end{cases} \quad (7)$$

is the transmitter's normalized flat-top pulse. We ignore the effects of atmospheric extinction and turbulence.

For a target that produces fully developed speckle statistics, the target field-reflection coefficient $T(\boldsymbol{\rho}'')$ is a complex-valued Gaussian random process with the following first- and second-order moments:^{3,8}

$$E_T[T(\boldsymbol{\rho}'')] = 0, \quad E_T[T(\boldsymbol{\rho}_1'')T(\boldsymbol{\rho}_2'')] = 0, \quad E_T[T^*(\boldsymbol{\rho}_1'')T(\boldsymbol{\rho}_2'')] = \lambda^2 \mathcal{T}(\boldsymbol{\rho}_1'') \delta(\boldsymbol{\rho}_1'' - \boldsymbol{\rho}_2'') \quad (8)$$

Similarly, the PSA input is in coherent state, conditioned on the target speckle, with a mean equal to:

$$\langle \hat{E}_{\text{PSA}}^{\text{in}}(\boldsymbol{\rho}, t) \rangle = \int A(\boldsymbol{\rho}') E_R(\boldsymbol{\rho}', t) \frac{e^{ik\boldsymbol{\rho} \cdot \boldsymbol{\rho}'/L}}{\lambda L} d\boldsymbol{\rho}' \quad (9)$$

$$= \sqrt{\frac{I_T \tau_p}{\hbar \omega}} s(t - 2L/c - F/c) \int T(\boldsymbol{\rho}'') m(\boldsymbol{\rho} - \boldsymbol{\rho}'') d\boldsymbol{\rho}'', \quad (10)$$

where we have dropped unimportant quadratic and absolute phase factors.

4.2 PSA output

Equation 3 shows the PSA input/output relationship. By properly choosing the temporal CON mode set $\{\xi_m(t)\}$ such that $\xi_1(t) = s(t - 2L/c - F/c)$, and since the detector applies a matched filter for $\xi_1(t)$, we can drop the time index and deal solely with the pure spatially-dependent field operators, as follows:

$$\hat{E}_{\text{PSA}}^{\text{in}}(\boldsymbol{\rho}) = \sum_n \hat{a}_n^{\text{in}} \Phi_n(\boldsymbol{\rho}) \quad (11)$$

$$\hat{E}_{\text{PSA}}^{\text{out}}(\boldsymbol{\rho}) = \sum_n \hat{a}_n^{\text{out}} \phi_n(\boldsymbol{\rho}) \quad (12)$$

$$\hat{a}_n^{\text{out}} = \sqrt{g_n} \hat{a}_n^{\text{in}} + \sqrt{g_n - 1} (\hat{a}_n^{\text{in}})^\dagger. \quad (13)$$

For this modal decomposition, we can write the PSA input-output relation as

$$\hat{E}_{\text{PSA}}^{\text{out}}(\boldsymbol{\rho}) = \int [\mu(\boldsymbol{\rho}, \boldsymbol{\rho}') \hat{E}_{\text{PSA}}^{\text{in}}(\boldsymbol{\rho}') + \nu(\boldsymbol{\rho}, \boldsymbol{\rho}') \hat{E}_{\text{PSA}}^{\text{in}}(\boldsymbol{\rho}')^\dagger] d\boldsymbol{\rho}', \quad (14)$$

where

$$\mu(\boldsymbol{\rho}, \boldsymbol{\rho}') = \sum_n \sqrt{g_n} \phi_n(\boldsymbol{\rho}) \Phi_n^*(\boldsymbol{\rho}'), \quad \nu(\boldsymbol{\rho}, \boldsymbol{\rho}') = \sum_n \sqrt{g_n - 1} \phi_n(\boldsymbol{\rho}) \Phi_n(\boldsymbol{\rho}') \quad (15)$$

For a given soft-aperture PSF $m(\boldsymbol{\rho})$, we define the functions

$$\mu^{(m)}(\boldsymbol{\rho}, \boldsymbol{\rho}'') = \int \mu(\boldsymbol{\rho}, \boldsymbol{\rho}') m(\boldsymbol{\rho}' - \boldsymbol{\rho}'') d\boldsymbol{\rho}', \quad \nu^{(m)}(\boldsymbol{\rho}, \boldsymbol{\rho}'') = \int \nu(\boldsymbol{\rho}, \boldsymbol{\rho}') m(\boldsymbol{\rho}' - \boldsymbol{\rho}'') d\boldsymbol{\rho}' \quad (16)$$

Then the PSA output mean, conditioned on the target speckle, is

$$\langle \hat{E}_{\text{PSA}}^{\text{out}}(\boldsymbol{\rho}) \rangle = \int [\mu(\boldsymbol{\rho}, \boldsymbol{\rho}') \langle \hat{E}_{\text{PSA}}^{\text{in}}(\boldsymbol{\rho}') \rangle + \nu(\boldsymbol{\rho}, \boldsymbol{\rho}') \langle \hat{E}_{\text{PSA}}^{\text{in}}(\boldsymbol{\rho}') \rangle^*] d\boldsymbol{\rho}' \quad (17)$$

$$= \sqrt{\frac{I_T \tau_p}{\hbar \omega}} \int [\mu^{(m)}(\boldsymbol{\rho}, \boldsymbol{\rho}'') T(\boldsymbol{\rho}'') + \nu^{(m)}(\boldsymbol{\rho}, \boldsymbol{\rho}'') T^*(\boldsymbol{\rho}'')] d\boldsymbol{\rho}'', \quad (18)$$

Let $\Delta \hat{E}_{\text{PSA}}^{\text{out}}(\boldsymbol{\rho}) \equiv \hat{E}_{\text{PSA}}^{\text{out}}(\boldsymbol{\rho}) - \langle \hat{E}_{\text{PSA}}^{\text{out}}(\boldsymbol{\rho}) \rangle$. Then the PSA output phase-insensitive and phase-sensitive conditional covariance functions $K^{(n)}(\boldsymbol{\rho}_1, \boldsymbol{\rho}_2|T)$ and $K^{(p)}(\boldsymbol{\rho}_1, \boldsymbol{\rho}_2|T)$ are equal to:

$$K^{(n)}(\boldsymbol{\rho}_1, \boldsymbol{\rho}_2|T) = \left\langle \int [\mu^*(\boldsymbol{\rho}_1, \boldsymbol{\rho}') \Delta \hat{E}_{\text{PSA}}^{\text{in}}(\boldsymbol{\rho}')^\dagger + \nu^*(\boldsymbol{\rho}_1, \boldsymbol{\rho}') \Delta \hat{E}_{\text{PSA}}^{\text{in}}(\boldsymbol{\rho}')] d\boldsymbol{\rho}' \right. \\ \left. \times \int [\mu(\boldsymbol{\rho}_2, \boldsymbol{\rho}'') \Delta \hat{E}_{\text{PSA}}^{\text{in}}(\boldsymbol{\rho}'') + \nu(\boldsymbol{\rho}_2, \boldsymbol{\rho}'') \Delta \hat{E}_{\text{PSA}}^{\text{in}}(\boldsymbol{\rho}'')^\dagger] d\boldsymbol{\rho}'' \right\rangle \quad (19)$$

$$= \int \nu^*(\boldsymbol{\rho}_1, \boldsymbol{\rho}') \nu(\boldsymbol{\rho}_2, \boldsymbol{\rho}') d\boldsymbol{\rho}'. \quad (20)$$

$$K^{(p)}(\boldsymbol{\rho}_1, \boldsymbol{\rho}_2|T) = \left\langle \int [\mu(\boldsymbol{\rho}_1, \boldsymbol{\rho}') \Delta \hat{E}_{\text{PSA}}^{\text{in}}(\boldsymbol{\rho}') + \nu(\boldsymbol{\rho}_1, \boldsymbol{\rho}') \Delta \hat{E}_{\text{PSA}}^{\text{in}}(\boldsymbol{\rho}')^\dagger] d\boldsymbol{\rho}' \right. \\ \left. \times \int [\mu(\boldsymbol{\rho}_2, \boldsymbol{\rho}'') \Delta \hat{E}_{\text{PSA}}^{\text{in}}(\boldsymbol{\rho}'') + \nu(\boldsymbol{\rho}_2, \boldsymbol{\rho}'') \Delta \hat{E}_{\text{PSA}}^{\text{in}}(\boldsymbol{\rho}'')^\dagger] d\boldsymbol{\rho}'' \right\rangle \quad (21)$$

$$= \int \mu(\boldsymbol{\rho}_1, \boldsymbol{\rho}') \nu(\boldsymbol{\rho}_2, \boldsymbol{\rho}') d\boldsymbol{\rho}'. \quad (22)$$

where the last two equalities follow since the PSA input $\hat{E}_{\text{PSA}}^{\text{in}}(\boldsymbol{\rho})$ is in a coherent state, so it has covariance functions $K_{\text{in}}^{(n)}(\boldsymbol{\rho}_1, \boldsymbol{\rho}_2|T) = K_{\text{in}}^{(p)}(\boldsymbol{\rho}_1, \boldsymbol{\rho}_2|T) = 0$.

4.3 Homodyne output: continuum detector case

We perform homodyne detection with a θ -phase plane-wave local oscillator, followed by a matched filter. All of the detector elements have quantum efficiency η , so we write

$$\hat{E}(\boldsymbol{\rho}, t) = \sqrt{\eta} \hat{E}_{\text{PSA}}^{\text{out}}(\boldsymbol{\rho}, t) + \sqrt{1 - \eta} \hat{E}_\eta(\boldsymbol{\rho}, t),$$

where $\hat{E}_\eta(\boldsymbol{\rho}, t)$ is a vacuum-state field. The output of the matched filter is

$$y_d(\boldsymbol{\rho}) = \int \text{Re}[\hat{E}(\boldsymbol{\rho}, t) e^{-i\theta}] s^*(t - 2L/c) dt \quad (23)$$

$$= \text{Re}[\hat{E}(\boldsymbol{\rho}) e^{-i\theta}] \quad (24)$$

$$= \sqrt{\eta} \text{Re}[\hat{E}_{\text{PSA}}^{\text{out}}(\boldsymbol{\rho}) e^{-i\theta}] + \sqrt{1 - \eta} \text{Re}[\hat{E}_\eta(\boldsymbol{\rho}) e^{-i\theta}] \quad (25)$$

$$= \sqrt{\eta} \text{Re}[\hat{E}_{\text{PSA}}^{\text{out}}(\boldsymbol{\rho}) e^{-i\theta}] + \sqrt{1 - \eta} \hat{e}_\eta(\boldsymbol{\rho}). \quad (26)$$

Note that the left-hand side of this equation is a classical random process whereas its right-hand side is a quantum operator. This notation is meant to convey that the statistics of the classical random process on the left-hand side coincide with the measurement statistics for the quantum operator on the right-hand side. Because the quantum operator on the right-hand side is in a zero-mean Gaussian state, we know that the classical random process on the left-hand side is zero-mean and Gaussian. To complete its statistical characterization, we now compute the mean and covariance of $y_d(\boldsymbol{\rho})$.

The matched filter output $y_d(\boldsymbol{\rho}) = s_d(\boldsymbol{\rho}) + n_d(\boldsymbol{\rho})$ where $s_d(\boldsymbol{\rho}) = \langle y_d(\boldsymbol{\rho}) \rangle$ is the target return and $n_d(\boldsymbol{\rho}) = \Delta y_d(\boldsymbol{\rho}) = y_d(\boldsymbol{\rho}) - \langle y_d(\boldsymbol{\rho}) \rangle$ represents the quantum noise. The target return $s_d(\boldsymbol{\rho})$ is a function of speckle $T(\boldsymbol{\rho}'')$ and is a classical zero-mean Gaussian random process. The noise component $n_d(\boldsymbol{\rho})$ is independent of speckle and is in also a zero-mean Gaussian random process.

The target return is $s_d(\boldsymbol{\rho}) = \langle y_d(\boldsymbol{\rho}) \rangle = \sqrt{\eta} \langle \text{Re}[\hat{E}_{\text{PSA}}^{\text{out}}(\boldsymbol{\rho})e^{-i\theta}] \rangle = \frac{\sqrt{\eta}}{2} [\langle \hat{E}_{\text{PSA}}^{\text{out}}(\boldsymbol{\rho}) \rangle e^{-i\theta} + \langle \hat{E}_{\text{PSA}}^{\text{out}}(\boldsymbol{\rho})^* \rangle e^{i\theta}]$. Thus, the target-return covariance is

$$K_s(\boldsymbol{\rho}_1, \boldsymbol{\rho}_2) = E_T[s_d(\boldsymbol{\rho}_1)s_d(\boldsymbol{\rho}_2)] \quad (27)$$

$$= \frac{\eta}{2} \text{Re} \left\{ E_T \left[\langle \hat{E}_{\text{PSA}}^{\text{out}}(\boldsymbol{\rho}_1) \rangle \langle \hat{E}_{\text{PSA}}^{\text{out}}(\boldsymbol{\rho}_2) \rangle \right] e^{-2i\theta} + E_T \left[\langle \hat{E}_{\text{PSA}}^{\text{out}}(\boldsymbol{\rho}_1) \rangle^* \langle \hat{E}_{\text{PSA}}^{\text{out}}(\boldsymbol{\rho}_2) \rangle \right] \right\} \quad (28)$$

$$= \frac{\eta}{2} \text{Re} \left\{ \frac{I_T \tau_p}{\hbar \omega} \lambda^2 \int \mathcal{T}(\boldsymbol{\rho}'') \left[\mu^{(m)}(\boldsymbol{\rho}_1, \boldsymbol{\rho}'') \nu^{(m)}(\boldsymbol{\rho}_2, \boldsymbol{\rho}'') + \mu^{(m)}(\boldsymbol{\rho}_2, \boldsymbol{\rho}'') \nu^{(m)}(\boldsymbol{\rho}_1, \boldsymbol{\rho}'') \right] d\boldsymbol{\rho}'' e^{-2i\theta} \right. \\ \left. + \frac{I_T \tau_p}{\hbar \omega} \lambda^2 \int \mathcal{T}(\boldsymbol{\rho}'') \left[\mu^{(m)}(\boldsymbol{\rho}_1, \boldsymbol{\rho}'')^* \mu^{(m)}(\boldsymbol{\rho}_2, \boldsymbol{\rho}'') + \nu^{(m)}(\boldsymbol{\rho}_1, \boldsymbol{\rho}'')^* \nu^{(m)}(\boldsymbol{\rho}_2, \boldsymbol{\rho}'') \right] d\boldsymbol{\rho}'' \right\}. \quad (29)$$

And using Eq. (4) to replacing $\mathcal{T}(\boldsymbol{\rho}'')$ we obtain that under H_1 ,

$$K_s(\boldsymbol{\rho}_1, \boldsymbol{\rho}_2) = K_1 \text{Re} \left(\left[\mu^{(m)}(\boldsymbol{\rho}_1, \mathbf{0}) \nu^{(m)}(\boldsymbol{\rho}_2, \mathbf{0}) + \mu^{(m)}(\boldsymbol{\rho}_2, \mathbf{0}) \nu^{(m)}(\boldsymbol{\rho}_1, \mathbf{0}) \right] e^{-2i\theta} \right. \\ \left. + \left[\mu^{(m)}(\boldsymbol{\rho}_1, \mathbf{0})^* \mu^{(m)}(\boldsymbol{\rho}_2, \mathbf{0}) + \nu^{(m)}(\boldsymbol{\rho}_1, \mathbf{0})^* \nu^{(m)}(\boldsymbol{\rho}_2, \mathbf{0}) \right] \right). \quad (30)$$

and under H_2 ,

$$K_s(\boldsymbol{\rho}_1, \boldsymbol{\rho}_2) = \frac{K_1}{2} \text{Re} \left(\left[\mu^{(m)}(\boldsymbol{\rho}_1, \theta_0 \mathbf{L} \mathbf{i}_{x''}) \nu^{(m)}(\boldsymbol{\rho}_2, \theta_0 \mathbf{L} \mathbf{i}_{x''}) + \mu^{(m)}(\boldsymbol{\rho}_2, \theta_0 \mathbf{L} \mathbf{i}_{x''}) \nu^{(m)}(\boldsymbol{\rho}_1, \theta_0 \mathbf{L} \mathbf{i}_{x''}) \right] e^{-2i\theta} \right. \\ \left. + \left[\mu^{(m)}(\boldsymbol{\rho}_1, \theta_0 \mathbf{L} \mathbf{i}_{x''})^* \mu^{(m)}(\boldsymbol{\rho}_2, \theta_0 \mathbf{L} \mathbf{i}_{x''}) + \nu^{(m)}(\boldsymbol{\rho}_1, \theta_0 \mathbf{L} \mathbf{i}_{x''})^* \nu^{(m)}(\boldsymbol{\rho}_2, \theta_0 \mathbf{L} \mathbf{i}_{x''}) \right] \right. \\ \left. + \left[\mu^{(m)}(\boldsymbol{\rho}_1, -\theta_0 \mathbf{L} \mathbf{i}_{x''}) \nu^{(m)}(\boldsymbol{\rho}_2, -\theta_0 \mathbf{L} \mathbf{i}_{x''}) + \mu^{(m)}(\boldsymbol{\rho}_2, -\theta_0 \mathbf{L} \mathbf{i}_{x''}) \nu^{(m)}(\boldsymbol{\rho}_1, -\theta_0 \mathbf{L} \mathbf{i}_{x''}) \right] e^{-2i\theta} \right. \\ \left. + \left[\mu^{(m)}(\boldsymbol{\rho}_1, -\theta_0 \mathbf{L} \mathbf{i}_{x''})^* \mu^{(m)}(\boldsymbol{\rho}_2, -\theta_0 \mathbf{L} \mathbf{i}_{x''}) + \nu^{(m)}(\boldsymbol{\rho}_1, -\theta_0 \mathbf{L} \mathbf{i}_{x''})^* \nu^{(m)}(\boldsymbol{\rho}_2, -\theta_0 \mathbf{L} \mathbf{i}_{x''}) \right] \right). \quad (31)$$

where $K_1 = \frac{\eta}{2} \frac{I_T \tau_p A_T}{\hbar \omega} \lambda^2$.

Similarly, the noise $n_d(\boldsymbol{\rho}) = \frac{\sqrt{\eta}}{2} \left(\Delta \hat{E}_{\text{PSA}}^{\text{out}}(\boldsymbol{\rho}) e^{-i\theta} + \Delta \hat{E}_{\text{PSA}}^{\text{out}}(\boldsymbol{\rho})^\dagger e^{i\theta} \right) + \sqrt{1-\eta} \hat{e}_\eta(\boldsymbol{\rho})$. Then noise covariance is

$$K_n(\boldsymbol{\rho}_1, \boldsymbol{\rho}_2) = \langle n_d(\boldsymbol{\rho}_1) n_d(\boldsymbol{\rho}_2) \rangle \quad (32)$$

$$= \frac{\eta}{2} \text{Re} \left\{ \langle \Delta \hat{E}_{\text{PSA}}^{\text{out}}(\boldsymbol{\rho}_1) \Delta \hat{E}_{\text{PSA}}^{\text{out}}(\boldsymbol{\rho}_2) \rangle e^{-2i\theta} + \langle \Delta \hat{E}_{\text{PSA}}^{\text{out}}(\boldsymbol{\rho}_1)^\dagger \Delta \hat{E}_{\text{PSA}}^{\text{out}}(\boldsymbol{\rho}_2) \rangle \right\} + \frac{1}{4} \delta(\boldsymbol{\rho}_1 - \boldsymbol{\rho}_2) \quad (33)$$

$$= \frac{\eta}{2} \text{Re} \left\{ K^{(p)}(\boldsymbol{\rho}_1, \boldsymbol{\rho}_2 | T) e^{-2i\theta} + K^{(n)}(\boldsymbol{\rho}_1, \boldsymbol{\rho}_2 | T) \right\} + \frac{1}{4} \delta(\boldsymbol{\rho}_1 - \boldsymbol{\rho}_2) \quad (34)$$

$$= \frac{\eta}{2} \text{Re} \left\{ \int \left[\mu(\boldsymbol{\rho}_1, \boldsymbol{\rho}') \nu(\boldsymbol{\rho}_2, \boldsymbol{\rho}') e^{-2i\theta} + \nu^*(\boldsymbol{\rho}_1, \boldsymbol{\rho}') \nu(\boldsymbol{\rho}_2, \boldsymbol{\rho}') \right] d\boldsymbol{\rho}' \right\} + \frac{1}{4} \delta(\boldsymbol{\rho}_1 - \boldsymbol{\rho}_2). \quad (35)$$

Param.	Pump size	Pump power	S_x	S_y	N_p	η	$MCruns$
Value	$400\mu m \times 25\mu m$	2.5 KWatts	0.5656	1.5373	15	0.25	10^7

Table 2: Default configuration parameters

4.4 Homodyne output: discrete-detector array case

We consider a discrete one dimensional array of N_p pixels of dimensions $D_x \times D_y$, as shown in Figure 2. The m -th detector in the array is centered at $\boldsymbol{\rho} = (mD_x, 0)$, for $-N_x \leq m \leq N_x$.

The output of the m -th detector is $y_m = \int_{\mathcal{A}_m} y_d(\boldsymbol{\rho}) d\boldsymbol{\rho}$. The $\{y_m\}$ are zero-mean jointly Gaussian random variables with covariance $E[y_m y_n] = E[s_m s_n] + E[w_m w_n]$. The target-return and noise covariances are

$$E[s_m s_n] = \int_{\mathcal{A}_m} \int_{\mathcal{A}_n} K_s(\boldsymbol{\rho}_1, \boldsymbol{\rho}_2) d\boldsymbol{\rho}_1 d\boldsymbol{\rho}_2 \quad (36)$$

$$E[w_m w_n] = \int_{\mathcal{A}_m} \int_{\mathcal{A}_n} K_n(\boldsymbol{\rho}_1, \boldsymbol{\rho}_2) d\boldsymbol{\rho}_1 d\boldsymbol{\rho}_2 \quad (37)$$

$$= \frac{\eta}{2} \int_{\mathcal{A}_m} \int_{\mathcal{A}_n} \text{Re} \left\{ \int [\mu(\boldsymbol{\rho}_1, \boldsymbol{\rho}') \nu(\boldsymbol{\rho}_2, \boldsymbol{\rho}') e^{-2i\theta} + \nu^*(\boldsymbol{\rho}_1, \boldsymbol{\rho}') \nu(\boldsymbol{\rho}_2, \boldsymbol{\rho}')] d\boldsymbol{\rho}' \right\} d\boldsymbol{\rho}_1 d\boldsymbol{\rho}_2 + \frac{D_x D_y}{4} \delta_{mn}. \quad (38)$$

Replacing (30), (31), and (35) above, and introducing the terms:

$$\begin{aligned} b_{kn} &= \int_{\mathcal{A}_n} \phi_k(\boldsymbol{\rho}) d\boldsymbol{\rho} & , & \quad m_k^{(0)} = \int m(\boldsymbol{\rho}) \Phi_k^*(\boldsymbol{\rho}) d\boldsymbol{\rho} \\ m_k^{(+)} &= \int m(\boldsymbol{\rho} + \theta_0 L \mathbf{i}_x) \Phi_k^*(\boldsymbol{\rho}) d\boldsymbol{\rho} & , & \quad m_k^{(-)} = \int m(\boldsymbol{\rho} - \theta_0 L \mathbf{i}_x) \Phi_k^*(\boldsymbol{\rho}) d\boldsymbol{\rho} \\ s_1^{n0} &= \sum_{k=1}^{k=50} \sqrt{g_k} m_k^{(0)} b_{kn} + \int_{\mathcal{A}_n} m_{residual}^{(0)}(\boldsymbol{\rho}) d\boldsymbol{\rho} & , & \quad s_2^{n0} = \sum_{k=1}^{k=50} \sqrt{g_k - 1} \left(m_k^{(0)} \right)^* b_{kn} \\ s_1^{n+} &= \sum_{k=1}^{k=50} \sqrt{g_k} m_k^{(+)} b_{kn} + \int_{\mathcal{A}_n} m_{residual}^{(+)}(\boldsymbol{\rho}) d\boldsymbol{\rho} & , & \quad s_2^{n+} = \sum_{k=1}^{k=50} \sqrt{g_k - 1} \left(m_k^{(+)} \right)^* b_{kn} \\ s_1^{n-} &= \sum_{k=1}^{k=50} \sqrt{g_k} m_k^{(-)} b_{kn} + \int_{\mathcal{A}_n} m_{residual}^{(-)}(\boldsymbol{\rho}) d\boldsymbol{\rho} & , & \quad s_2^{n-} = \sum_{k=1}^{k=50} \sqrt{g_k - 1} \left(m_k^{(-)} \right)^* b_{kn} \end{aligned}$$

it can be shown that

$$E[s_m s_n] = \begin{cases} K_1 \text{Re} \{ e^{-2i\theta} (s_1^{n0} s_2^{m0} + s_2^{n0} s_1^{m0}) + (s_1^{n0})^* s_1^{m0} + (s_2^{n0})^* s_2^{m0} \} & \text{under } H_1 \\ 0.5 \times K_1 \text{Re} \{ e^{-2i\theta} (s_1^{n+} s_2^{m+} + s_2^{n+} s_1^{m+} + s_1^{n-} s_2^{m-} + s_2^{n-} s_1^{m-}) \\ \quad + (s_1^{n+})^* s_1^{m+} + (s_2^{n+})^* s_2^{m+} + (s_1^{n-})^* s_1^{m-} + (s_2^{n-})^* s_2^{m-} \} & \text{under } H_2, \end{cases} \quad (39)$$

and

$$E[w_m w_n] = \frac{\eta}{2} \text{Re} \left\{ \sum_{k=1}^{k=50} \sqrt{g_k (g_k - 1)} b_{km} b_{kn} + (g_k - 1) b_{km}^* b_{kn} \right\} + \frac{D_x D_y}{4} \delta_{mn} \quad (40)$$

where $m_{residual}^{(0)}(\boldsymbol{\rho})$, $m_{residual}^{(+)}(\boldsymbol{\rho})$, and $m_{residual}^{(-)}(\boldsymbol{\rho})$ represent the portion of $m(\boldsymbol{\rho})$, $m(\boldsymbol{\rho} + \theta_0 L \mathbf{i}_x)$, and $m(\boldsymbol{\rho} - \theta_0 L \mathbf{i}_x)$ (respectively) that is orthogonal to the space spanned by the first 50 eigenmodes.

5. NUMERICAL RESULTS

In this section we present our numerical results. We also briefly discuss the rationale behind the observed PSA behavior. In many cases our realistic spatial bandwidth limited model will be compared with the flat-phase ‘‘infinite-bandwidth’’ approximation device (with all modes amplified in the homodyne quadrature) discussed in the introduction. There are several surprising results in which the non-uniform phase behavior of the realistic model leads to better performance of the flat-phase infinite-bandwidth model.

It should be noted that there are several degrees of freedom over which performance can be optimized, including pump geometry/size, pump power, pixel size (width and height), number of pixels, and lenses focus in x- or y-dimension. What we found is that for a given pump size, a good strategy is to independently adjust

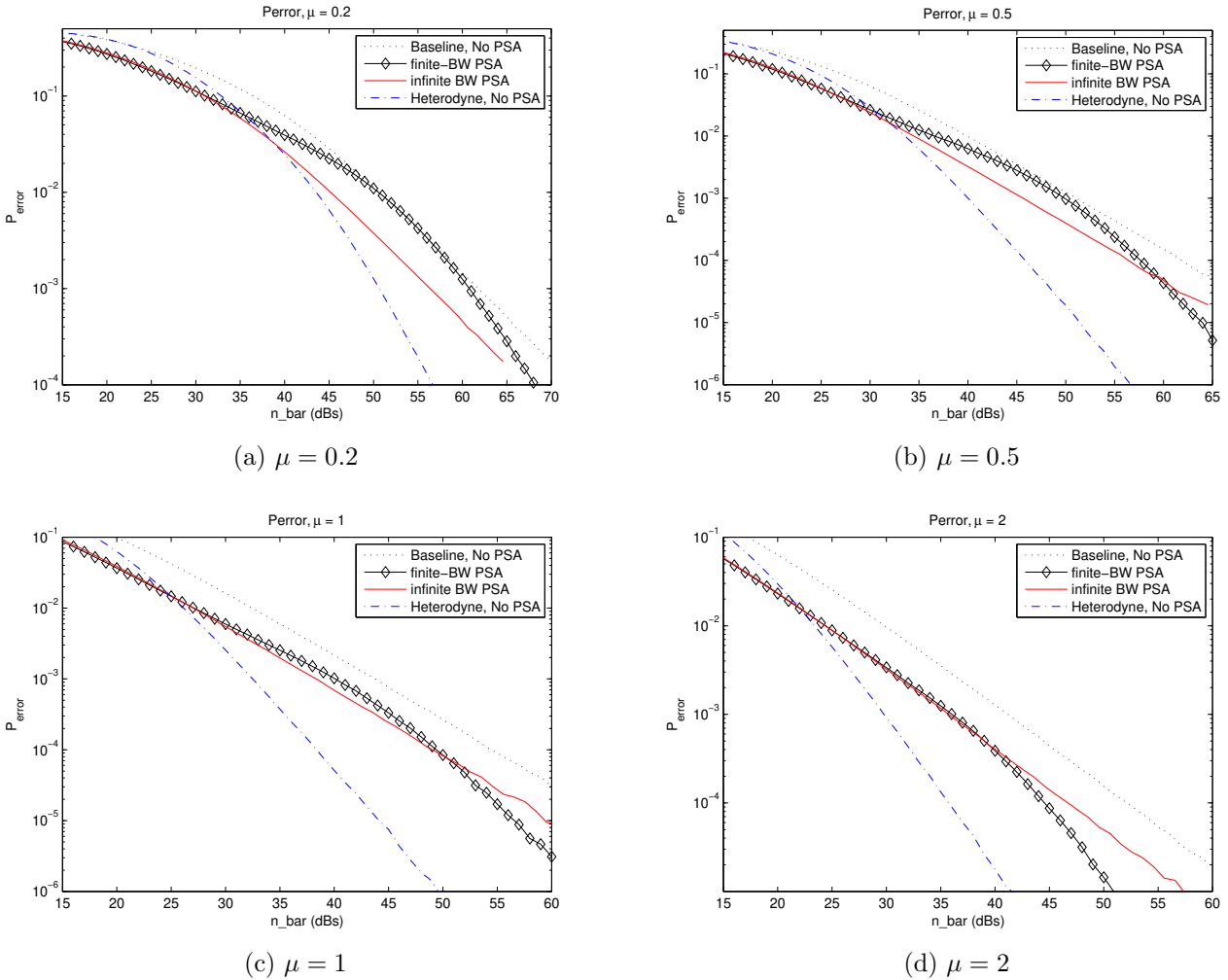


Figure 6: (Color Online) Error probability for the 1-versus-2 target hypothesis testing for different (normalized) angular separations.

the X- and Y-focus such that the 1-target signal matches the real part of the PSA’s most amplified eigenmode. Furthermore, there is a relation between the pixel width and the aperture spatial resolution (similar to Nyquist sampling). Roughly speaking, the pixel width (in dimensionless units S_x) must be less than 1 in order to prevent further loss of resolution. For the pixel height (S_y in dimensionless units) we found that while there is an optimal operating point, the system has very little sensitivity to even large deviations from it. Thus, choosing the right value for S_y is of little impact. Table 2 shows the default configuration parameters that were used – unless explicitly noted – to derive the results presented in this paper.

5.1 Error probability versus \bar{n}

Figure 6 shows the detection error probability, computed using Monte Carlo (MC) simulations (10^7 runs), for several values of target separation (μ). The solid black line (with diamond markings) corresponds to the detection error probability obtained when our realistic model of the PSA is employed. For comparison, the red curve shows the expected performance under the “infinite-bandwidth” approximation. Also, as a reference, the blue dash line show the performance of a heterodyne detector without PSA pre-amplification. We can distinguish 3 different operating regions: (i) at low SNR, the finite-bandwidth PSA performance is very close

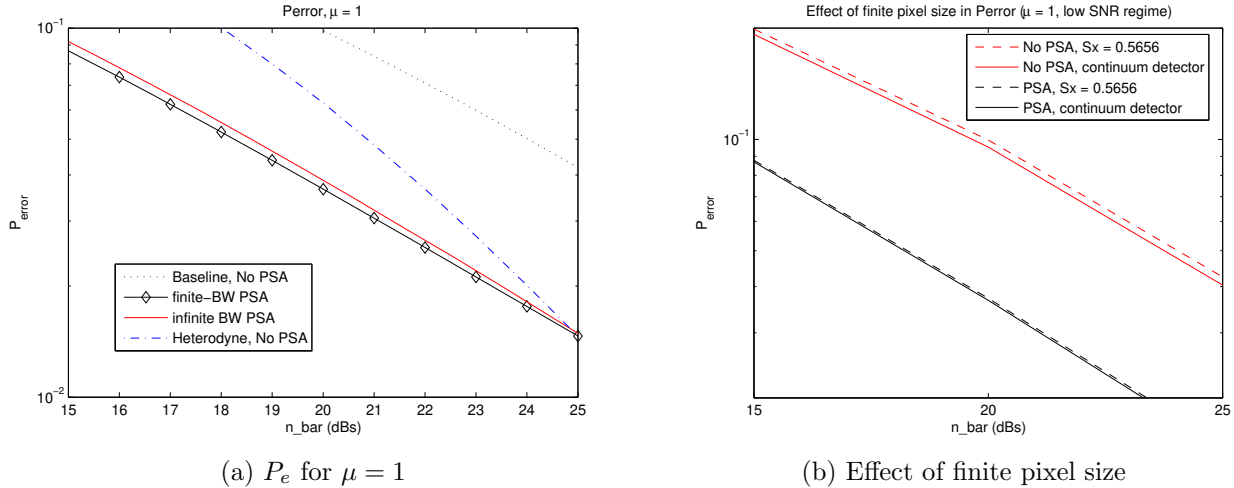


Figure 7: PSA outperforms infinite-bandwidth amplifier at low SNR. (a) P_e for $\mu = 1$, zooming-in for the low SNR regime. (b) Effect of finite pixel size ($S_x = 0.5656$). While the PSA-enhanced system suffers little degradation, the baseline system (no-PSA) loses close to 0.3 dB in performance with respect to the continuum detection array (i.e., $S_x \rightarrow 0$) case.

(slightly better) than an infinite bandwidth amplifier; (ii) at medium SNR, the finite-bandwidth performance degrades and for some values of μ and \bar{n} it provides no gain over the baseline (i.e., homodyne detector without PSA pre-amplification); and (iii) at high SNR, finite bandwidth asymptotic behavior is similar to a heterodyne detector and significantly outperforms an infinite-bandwidth amplifier as SNR increases. We will discuss the PSA-enhanced system behavior of each of these regions next.

5.2 Low SNR regime

Figure 7(a) shows a zoom-in on the probability of error curve for $\mu = 1$ for low values of \bar{n} (i.e. low SNR case). There it can be seen that the performance of a detector with a finite-bandwidth PSA pre-amplification is better than the expected value for an infinite value amplifier and (not shown) with the same gain as the PSA highest gain ($G_{eff,1}$). This behavior can be counterintuitive, as the initial expectation is that the spatial-bandwidth limitation of the PSA would result in signal distortion, loss of resolution, and lower detector gain. Instead, performance has actually improved. There are two main drivers for this good PSA performance.

Firstly, with the right focusing the target signal for the 1-target case (i.e. $m(\boldsymbol{\rho})$) is a very good match to the real part of the PSA first fundamental mode (both are Gaussian beams). Since this mode experiences the highest gain, the 1-target signal experiences close to optimal amplification, that is, there is no spatial distortion of the 1-target signal intensity function*. Furthermore, for most values of μ in the range of interest, the 2-target signals $m(\boldsymbol{\rho} + \theta_0 \mathbf{L}\mathbf{i}_x)$, and $m(\boldsymbol{\rho} - \theta_0 \mathbf{L}\mathbf{i}_x)$ have most of their energy in the space spanned by the first 3 most amplified eigenmodes. Since these eigenmodes' gains is still large, the 2-target signal also experiences close-to-optimal amplification.

Secondly, the PSA performs an all-optical filtering of out-of-band noise. Since the gains for higher order eigenmodes decreases rapidly, noise contributions associated with higher-order eigenmodes are significantly reduced (compared to a infinite bandwidth amplifier, where all the modes are equally amplified). Note that, as mentioned above, higher order eigenmodes carry little-to-no target signal information, and therefore the PSA preference for lower-index eigenmodes (where the signal resides) over higher-index ones (mostly noise contribution) results in a type of all-optical signal-matched filter. Note that an equivalent filtering can be applied in the electronic domain (i.e. post-processing using the covariance matrices) if and only if the detector array is continuum (zero pixel width) array of sufficient area. This explains the finite-bandwidth PSA advantage for

*The phase, however, will be distorted/conjugated.

practical (finite) pixel widths. For example, Figure 7(b) shows a comparison of the performance impact of the pixel size for a PSA-enhanced detector (black, finite bandwidth) and the baseline system (red, no PSA, infinite bandwidth). The solid lines show the performance when a continuum detector array is used. The dashed lines show the performance when a discrete pixel array (with $S_x = 0.5656$) is employed. It can be seen that the finite-bandwidth PSA system experiences negligible degradation, while the baseline system experiences a degradation of roughly 0.3dB . The main culprit for this performance degradation is the inability of the infinite bandwidth system to completely filter out out-of-band noise when the pixel size is non-negligible. Said in other words, while the different noise contributions are orthogonal at the input of the detector plane, the nature of the homodyne measurements (i.e., field integration over non-zero width pixels) does not preserve this orthogonality. Instead, different noise contribution become correlated with the target signal (i.e. fall “in-band”), and the output signal-to-noise ratio effectively increases. Note that since the finite-bandwidth PSA performs its noise pre-filtering *before* the homodyne measurement, it doesn’t suffer from this effect.

5.3 Medium SNR regime

As shown in Figure 6, the PSA-enhanced system worst relative performance occurs at medium SNR. The PSA-enhanced system performance degrades significantly, and in some cases (i.e. $\mu = 0.5$ and \bar{n} in Figure 6(b)) it may provide no benefit over a homodyne receiver without a PSA.

This behavior cannot be fully explained by the PSA’s finite spatial-bandwidth. Our analysis (see Section 5.5) shows that increasing the PSA spatial bandwidth (by utilizing a broadened pump) does not, in general, improve performance at medium SNR. Moreover, any finite bandwidth effect (gain reduction, filtering, etc.) should result in a constant loss (in dB), that is, the error curve should run parallel to the curve determined under the infinite bandwidth assumption. However, this is not the observed behavior. As can be seen in Figure 6, in all cases the PSA-enhance system’s error curve has a lower slope (lower rate of decay) than the infinite-bandwidth case (either infinite bandwidth PSA, or baseline) and its relative performance worsens as the SNR is increased.

5.4 High SNR regime

In the previous subsection we noticed that for medium SNR values the error curve slope for a PSA-enhanced system decays slower than the baseline. Let alone, this would imply that asymptotically the behavior of the PSA-enhanced system is much worse than the baseline. Fortunately, as shown in Figure 6, at a high enough SNR, an inflection point occurs and the slope of the error curve increases significantly. Comparing the 4 plots in Figure 6, it is evident that the slope of the error curve for the PSA-enhanced system is the same as (or very close to) the slope of a heterodyne receiver.

This initially surprising result is due to the spatial pattern of the PSA spatial output changing in response to changes on the phase of the input signal. At high SNR, the modification is noticeable and a detector can recover phase information. Furthermore, since the most amplified eigenmode is complex with its real and imaginary parts being linearly independent, the real component of the PSA output (measured by the homodyne detector array) is never zero. In contrast, without a finite-bandwidth PSA, the homodyne detector output is zero when the input signal is exactly 90 degrees out-of-phase.

To visualize that a PSA pre-amplified homodyne detector can recover phase information, let’s consider the following example: assume the target signal corresponds to the 1-target hypothesis and, for argument sake, let’s assume that the PSA has a single eigenmode $\Phi_1(\boldsymbol{\rho}) = V_{re}(\boldsymbol{\rho}) + jV_{im}(\boldsymbol{\rho})$. Of course, this is not a realistic assumption, but it serves to illustrate the way phase/quadrature information can be recovered. Let the input to the PSA (for a given speckle) be $(a_{re} + ja_{im}) \frac{m_1^{(0)}}{|m_1^{(0)}|} m(\boldsymbol{\rho})$, where $m_1^{(0)}$ is as before, the projection of $m(\boldsymbol{\rho})$ over the first input eigenmode $\Phi_1(\boldsymbol{\rho})$. The term $\frac{m_1^{(0)}}{|m_1^{(0)}|}$ is a unit amplitude phase scaling factor used to simplify the analysis. It follows that the target return at the output of a homodyne continuum detector is given by:

$$s_d(\boldsymbol{\rho}) = |m_1^{(0)}| \left(\sqrt{G_{eff,1}} a_{re} V_{re}(\boldsymbol{\rho}) + \frac{1}{\sqrt{G_{eff,1}}} a_{im} V_{im}(\boldsymbol{\rho}) \right) = VA^{-1} \bar{a} \quad (41)$$

where $V = [V_{re}(\boldsymbol{\rho})V_{im}(\boldsymbol{\rho})]^\dagger$, $\bar{a} = [a_{re} \ a_{im}]^T$ is the vector we are trying to estimate, and A is a 2×2 constant diagonal matrix accounting for PSA attenuation: $A_{11} = 1/(|m_1^{(0)}|\sqrt{G_{eff,1}})$, $A_{22} = \sqrt{G_{eff,1}}/|m_1^{(0)}|$, and $A_{12} = A_{21} = 0$.

Let's define the operator $\langle a, b \rangle = a^T b = \int a(\boldsymbol{\rho})b(\boldsymbol{\rho})d\boldsymbol{\rho}$ over the L^2 space. Then, since conditioned in the speckle the measurement are Gaussian variables, a good estimator for \bar{a} is the least squares estimator characterized by the linear operator $\mathcal{L} = AR^{-1}V^T$, where:

$$R = V^T V = \begin{bmatrix} f_{11} & f_{12} \\ f_{12} & f_{22} \end{bmatrix} \quad (42)$$

is the cross-correlation matrix (symmetric since the functions are real-valued) for the functions $(V_{re}(\boldsymbol{\rho}), V_{im}(\boldsymbol{\rho}))$. f_{11} is the energy of $V_{re}(\boldsymbol{\rho})$ and f_{22} is the energy of $V_{im}(\boldsymbol{\rho})$ and it follows that $f_{11} + f_{22} = 1$. Note that if $V_{re}(\boldsymbol{\rho})$ and $V_{im}(\boldsymbol{\rho})$ are linearly independent, then the matrix R is invertible.

The noise signal $n_d(\boldsymbol{\rho})$ at the output of the detector has three statistically independent components: one associated with vacuum noise, and two equal weighted terms associated with $V_{re}(\boldsymbol{\rho})$ and $V_{im}(\boldsymbol{\rho})$, as explained before. Treating $n_d(\boldsymbol{\rho})$ as a column vector, we can write

$$E\{n_d(\boldsymbol{\rho})n_d^T(\boldsymbol{\rho})\} = c_1 I + \frac{c_2}{2} V_{re} V_{re}^T + \frac{c_2}{2} V_{im} V_{im}^T = c_1 I + \frac{c_2}{2} V V^T$$

Finally, using the operator \mathcal{L} over the measurements $y_d(\boldsymbol{\rho}) = s_d(\boldsymbol{\rho}) + n_d(\boldsymbol{\rho})$ we obtain:

$$\mathcal{L}\{y_d(\boldsymbol{\rho})\} = AR^{-1}V^T V A^{-1} \bar{a} + N = \bar{a} + N$$

where $N = R^{-1}V^T n_d(\boldsymbol{\rho})$ is a zero-mean Gaussian random 2-dimensional vector with covariance matrix equal to

$$\begin{aligned} E\{N N^T\} &= AR^{-1}V^T E\{n_d(\boldsymbol{\rho})n_d^T(\boldsymbol{\rho})\} V R^{-1} A = AR^{-1}V^T (c_1 I + \frac{c_2}{2} V V^T) V R^{-1} A \\ &= c_1 A R^{-1} (V^T V) R^{-1} A + \frac{c_2}{2} A R^{-1} (V^T V) (V^T V) R^{-1} A = c_1 A R^{-1} A + \frac{c_2}{2} I_2 A^2 \end{aligned}$$

where the first term corresponds to the vacuum noise "amplified" by the matrix $AR^{-1}A$. The second term is the original eigenmode-related noise component, with the real and imaginary quadrature components amplified by the factors A_{11}^2 and A_{22}^2 respectively.

Thus, we can see that as long as the matrix R is invertible, it is possible to recover both quadrature values in \bar{a} . However, the price to pay is an increase in the noise level, as determined by the matrix $AR^{-1}A$.

For example, let's consider the case where the real and imaginary components of the fundamental eigenmode are orthogonal and of equal energy (i.e. $f_{11} = f_{22} = 0.5$ and $f_{12} = 0$). Then $R = 0.5I_2$ and $E\{N N^T\} = (2c_1 + c_2/2)A^2$, that is, the two noise terms are uncorrelated. This results in statistics fairly similar to a heterodyne detector, but with an decrease of the SNR for the imaginary component by a factor $A_{22}^2 = (G_{eff,1}/|m_1^{(0)}|)^2$ (roughly speaking, a SNR loss of the same order of magnitude of the PSA squeezing factor).

In practice, our values of f_{11} are close to 1 (e.g. 0.9734 for the default PSA parameters) and therefore there is a significant additional SNR loss when determining the quadrature information, which explains the large gap between the PSA-enhanced system and the heterodyne detector.

The explanation above is not intended to be rigorous, but illustrative of how if the set of real and imaginary components of the eigenmodes are linearly independent, then it is possible to recover phase information, although at a loss.

Moreover, it has been recently shown that the right modal transformation (i.e., unity gain, orthonormal real and imaginary components of output modes) just before a homodyne detector can convert the statistics of the homodyne detector output to those of a heterodyne detector.⁹

5.5 Effect of pump width/spatial bandwidth

In this section we investigate if the cause for the bad behavior at medium SNR is due to limited spatial bandwidth, and investigate the effect of changing the pump geometry.

[†]Note that for simplicity of description, $V_{re}(\boldsymbol{\rho})$ and $V_{im}(\boldsymbol{\rho})$ are being treated as infinite length column vector.

A broader pump has higher spatial bandwidth, which in theory should lead to better performance. Figure 8 compares the quadrature gains ($G_{eff,n}$) for two pump sizes ($800\mu\text{m} \times 25\mu\text{m}$ and $400\mu\text{m} \times 25\mu\text{m}$) under the *same illuminance*, i.e., the broader pump is excited with twice the power as the shorter one. It can be seen that the gain for the first eigenmode is the same in both cases, but the rate of decay is slower for the broader pump (higher spatial bandwidth).

Figure 9 shows the error probabilities for two values of μ . It can be seen that at low SNR, having a broader pump results in a slight improvement in performance. However, at high SNR, the higher-spatial bandwidth results in performance degradation. A possible explanation for this is the "heterodyne-like" behavior of the PSA-enhanced system at high SNR: a higher gain $G_{eff,n}$ for the signal real component implies a higher squeezing ($\frac{1}{G_{eff,n}}$) for the quadrature (imaginary) component. Since the availability of a quadrature component is the dominant factor for the observed low probability of error, any attenuation of the quadrature component will result in an increase in the error probability.

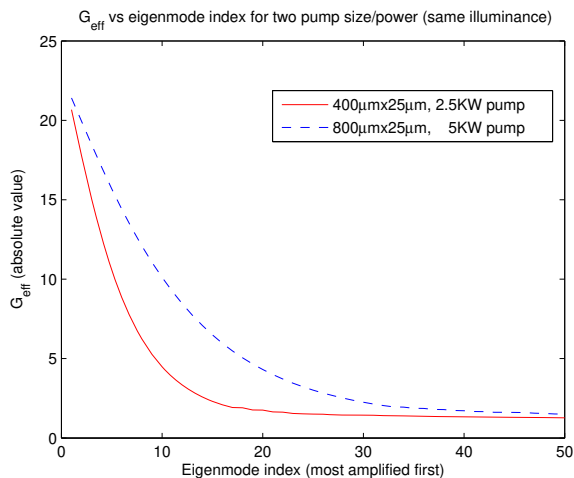
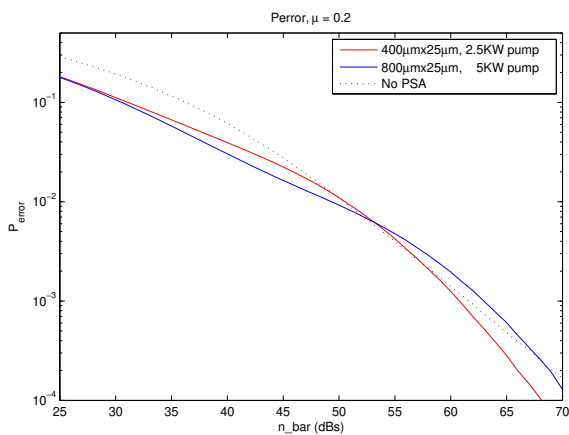
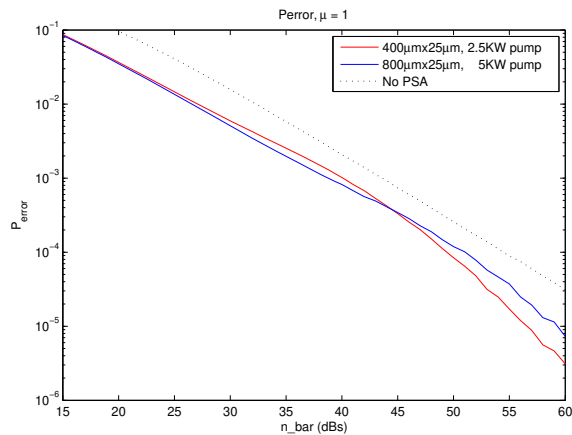


Figure 8: PSA quadrature gains vs eigenmode index for two different pump sizes. Illuminance (per area power) kept constant.



(a) $\mu = 0.2$



(b) $\mu = 1$

Figure 9: (Color Online) Error probability for the 1-versus-2 target hypothesis testing for different (normalized) angular separations for two different values of pump width.

It is instructive to calculate the target separation μ at which the error rate falls below some threshold probability of error P_{error} . Plotting this versus \bar{n} reveals a resolution curve. Finally, Figure 10 show the resolution curves for 4 different target error probabilities. It can be seen that for low and high error probability targets, there is little value in increasing the spatial bandwidth. Only for error probability in the order of 3×10^{-3} and for angular separation above 0.5 times the Rayleigh angular resolution, it is worthwhile to spent the extra power required to maintain a constant illuminance while increasing the pump width.

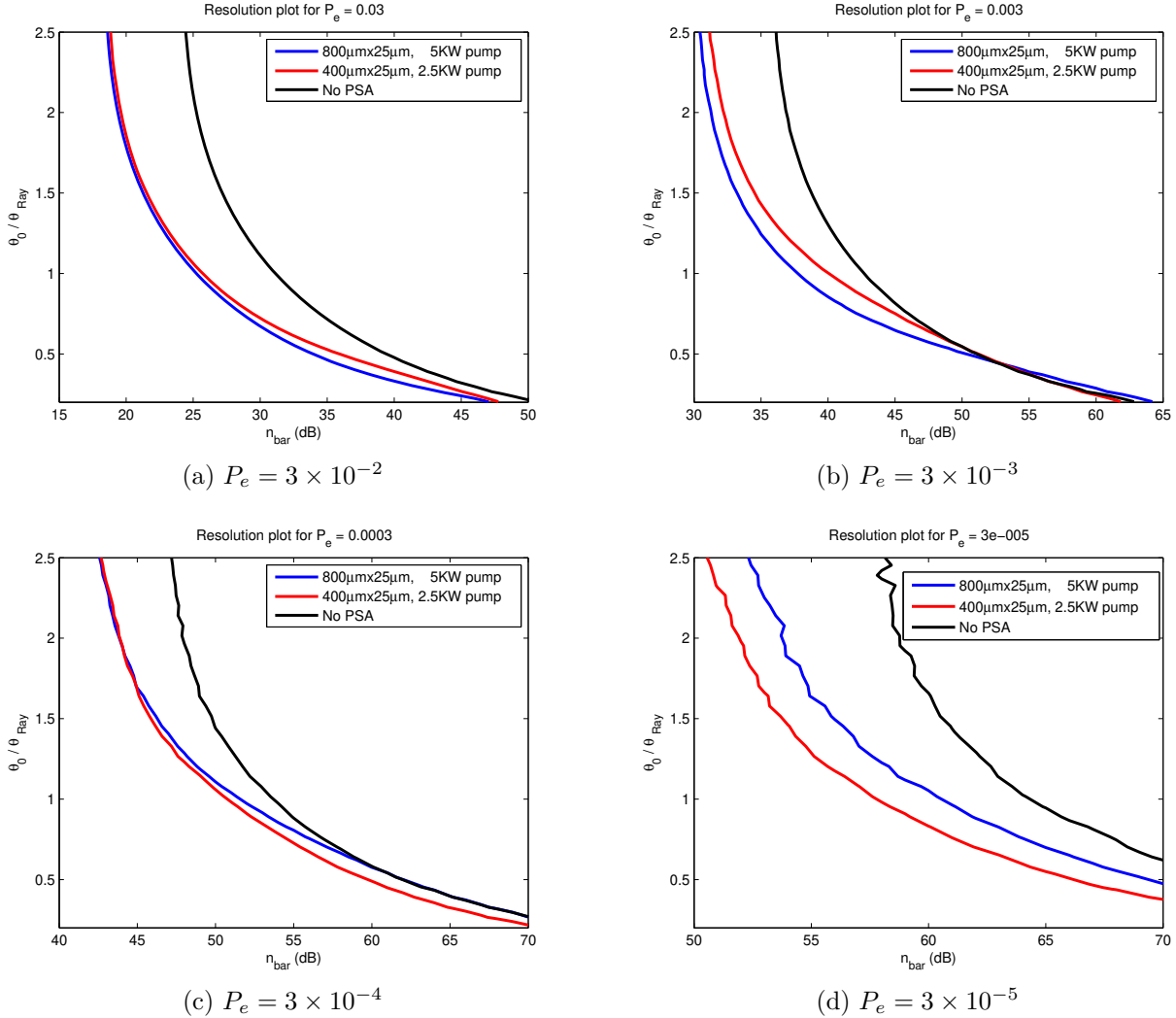


Figure 10: (Color Online) Resolution curves for different target error probabilities P_{error} for two different values of pump widths: $800\mu\text{m}$ (blue line) and $400\mu\text{m}$ (red line). Baseline (no PSA) shown in black. The broader pump, with higher spatial bandwidth, has better performance only in a limited number of cases.

6. DISCUSSION

In this paper we performed a complete characterization of a PSA crystal and compared its performance against the results obtained under the “infinite-spatial-bandwidth” assumption. We have found that under both low and high SNR, the performance of a PSA is better than the one predicted by the infinite-bandwidth, infinite gain assumption. But, at medium values of SNR, the PSA performance may be much worse than one predicted by the infinite-bandwidth assumption, and for certain values of μ it may even be worse than the performance of a system without a PSA (i.e. baseline system).

At low SNR, the good behavior of the PSA is due to (i) a good matching between the target signal and the PSA first fundamental modes (both are Gaussian beams) which result in little – if any – loss due to the PSA finite-bandwidth (i.e. signal excites the right modes), and (ii) the PSA behaving as an all-optical pre-filtering of out-of-band noise – which can only be duplicated in the electronic domain if the detector array is continuum (zero pixel width) and of sufficient area.

At medium SNR, however, we have observed some significant performance degradation. This cannot be fully explained by the PSA finite spatial-bandwidth. Our analysis shows that increasing the PSA spatial bandwidth (by utilizing a broader pump) does not, in general, improve performance at medium SNR. Moreover, any finite bandwidth effect (gain reduction, filtering, etc.) should result in a constant loss (in dB), that is, the error curve should run parallel to the curve determined under the infinite bandwidth assumption. However, this is not the observed behavior. Instead, the PSA error curve has a lower slope (lower rate of decay) than the infinite-bandwidth case, and its relative performance worsens as the SNR is increased. For some values of μ and SNR, the performance of the PSA can even be worse than the performance of a system without a PSA (i.e. baseline system).

At high SNR, the PSA good behavior is due to the PSA capability to recover some phase information. The PSA input/output modal transformation result in some quadrature (imaginary) component information being propagated (though squeezed) through the PSA. As the energy of this quadrature component grows above the noise floor, its availability dominates the error probability, overcoming the effects observed at medium SNR, and resulting in an error curve that asymptotically follows that of a heterodyne receiver.

In the future, we will further investigate the effect of the PSA modal transformation (i.e. output modes are the complex conjugate of the input modes) in the behavior observed at medium SNR, looking for guidelines for pump design (shape and/or power). Similarly, we will try to derive expressions relating the PSA behavior at high SNR with that of a heterodyne detector system (i.e. quantifying the dB gap).

ACKNOWLEDGMENTS

This work was supported by the DARPA Quantum Sensors Program under AFRL contract FA8750-09-C-0194. We thank Prem Kumar, Horace Yuen, Geoff Burdge, Jon Habif, John Myers, and P. Bidigare for useful discussions.

REFERENCES

- [1] G. W. Kamerman, ed., *Selected Papers on LADAR, SPIE Milestone Series, vol. MS133* (SPIE, Bellingham 1997).
- [2] G. R. Osche, *Optical Detection Theory for Laser Applications* (Wiley-Interscience, Hoboken, 2002).
- [3] Z. Dutton, J. H. Shapiro, and S. Guha, "LADAR resolution improvement using receivers enhanced with squeezed-vacuum injection and phase-sensitive amplification," *J. Opt. Soc. Am. B*, **27**, A63-A72 (2010).
- [4] M. Annamalai, N. Stelmakh, M. Vasilyev, and P. Kumar, "Eigenmodes of a travelling-wave phase-sensitive optical parametric amplifier," in *Proceedings of the 10th International Conference on Fibre Optics and Photonics: PHOTONICS-2010*, December 12-15, 2010, Indian Institute of Technology - Guwahati (IIT-G), India, paper 193.
- [5] M. Annamalai, N. Stelmakh, M. Vasilyev, P. Kumar, "Spatial Modes of Phase-Sensitive Image Amplifier with Elliptical Gaussian Pump," in *Proceedings of Frontiers in Optics / Laser Science XXVI conference*, October 24-28, 2010, Rochester, NY, paper LTuB5.
- [6] M. Vasilyev, M. Annamalai, N. Stelmakh, and P. Kumar, "Quantum properties of a spatially-broadband traveling-wave phase-sensitive optical parametric amplifier," *J. Mod. Opt.*, **57**, 1908-1915 (2010).
- [7] M. Annamalai, M. Vasilyev, N. Stelmakh, and P. Kumar, "Compact Representation of Spatial Modes of Phase-Sensitive Image Amplifier," in *Proceedings the Conference on Lasers and Electro-Optics*, Baltimore, MD, May 1-6, 2011, paper JThB77.
- [8] J. H. Shapiro, B. A. Capron, and R. C. Harney, "Imaging and target detection with a heterodyne-reception optical radar," *Appl. Opt.*, **20**, 3292-3313 (1981).
- [9] J. H. Shapiro, "Converting one-versus-two continuum homodyne detection into one-versus-two continuum heterodyne detection via pre-detection unitary transformation," Internal Memorandum, MIT, April 5, 2011.